Wake Recovery Enhancement with Helix Active Wake Control
Vortex Structures in a Porous Disk Wake Observed in PIV Experiments

Gutknecht, Jonas; Van Den Berg, Daniel; Van Der Hoek, Daan; De Vos, Brian; Harder, Bjorn; Viré, Axelle; Van Wingerden, Jan Willem

DOI
10.1088/1742-6596/3016/1/012030

Publication date
2025

Document Version
Final published version

Published in
Journal of Physics: Conference Series

Wake Recovery Enhancement with Helix Active Wake Control: Vortex Structures in a Porous Disk Wake Observed in PIV Experiments

Journal of Physics: Conference Series **3016** (2025) 012030 doi:10.1088/1742-6596/3016/1/012030

Wake Recovery Enhancement with Helix Active Wake Control: Vortex Structures in a Porous Disk Wake Observed in PIV Experiments

Jonas Gutknecht[1], Daniel van den Berg[1], Daan van der Hoek[1], Brian de Vos[1], Bjorn Harder[1], Axelle Viré[2], and Jan-Willem van Wingerden[1]

[1]Delft University of Technology, DCSC, Mekelweg 2, 2628 CD Delft, The Netherlands
[2]Delft University of Technology, Wind Energy Section, Kluyverweg 1, 2629 HS Delft, The Netherlands

E-mail: J.Gutknecht@tudelft.nl

Abstract. Power losses at waked turbines due to the energy extraction of upstream turbines from the flow pose a major risk to the economic feasibility of wind farms. Helix active wake control has proven its potential to mitigate these wake-induced power losses by accelerating the recovery of the individual turbine wakes. This method leverages individual pitch control to induce a non-uniformly distributed force perturbation that rotates either in a clockwise (CW) or counterclockwise (CCW) direction around the rotor center. This deforms the wake into a helical shape that recovers faster than the wake of a conventionally controlled turbine. The CCW-oriented helix achieves higher power gains than the CW helix. Previous studies have identified a system of counter-rotating vortices to drive the wake recovery enhancement and the difference between CW and CCW helix. Nevertheless, a causal explanation for the creation of these vortices is still pending. This work contributes to understanding their creation by isolating the effect of the helix force perturbation on a symmetric wake from the impact of blade-related features like tip-vortices, hub vortex, or wake swirl. For this purpose, we perform Particle Image Velocimetry (PIV) measurements of a porous disc (PD) model in a wind tunnel. The PD is modified to mimic the helix but does not inherit the blade-related features present in a wind turbine wake. We observe the formation of two counter-rotating vortices in the far wake that deform the wake cross-section into a kidney shape, analogous to the structures present in the wake when helix active wake control is applied to a wind turbine. A conceptual comparison of PD wake and wind turbine wake implies that the wake swirl present in the turbine wake causes asymmetric reactions in several characteristics of the vortex system to changes in the rotational direction of the helix perturbation. Consequently, the dynamic, non-uniform helix perturbation alone is sufficient to activate the governing mechanisms that enhance the wake recovery when using helix active wake control, while blade-related phenomena are not fundamental to the principal processes.

1 Introduction

Adhering to the conservation of energy principle, a wind turbine converts kinetic energy from the wind into electric energy, leaving a deficit of kinetic energy in its downstream region, the so-called wake. Clustering multiple turbines in close vicinity to form wind farms makes conditions in which some turbines operate in the wake of a neighboring ones inevitable. In these conditions, the waked turbines have a reduced energy input available for extraction, leading in extreme cases to a decrease in power production by up to 40 % [1] compared to a turbine exposed to the undisturbed wind. Those power losses cumulate throughout the farm, posing a major challenge to the economic profitability of wind farms.

Several methodologies have been developed to mitigate wake-induced power losses. Promising results were achieved by redirecting the wake away from downstream turbines by misaligning the turbine yaw from the incoming wind [2, 3, 4, 5]. Other strategies aim to accelerate the recovery of the velocity deficit in the wake by increasing its mixing with the surrounding flow. Therefore, they introduce periodic perturbations created by dynamic control signals at the turbine into the flow. The first methodology of that kind, known as pulse, was presented by Munters and Meyers [6], which imposes sinusoidal excitations on the turbine thrust. This triggers the periodic shedding of vortex rings from the rotor tips, which accelerates the wake mixing processes and thereby increases the farm-wide power output by up to 5 %. Addressing the increased power fluctuations that come along with the power gains of the pulse, Frederik et. al [7] presented helix active wake control. Instead of varying the thrust uniformly over the rotor plane, the helix increases the thrust on one side and reduces it on the other side by locally adapting the individual blade pitch angle as it sweeps over the rotor plane. Additionally, the nonuniform thrust distribution rotates around the rotor center, which is achieved by offsetting the blade pitch frequency from the rotational speed of the rotor. Experimental investigations in wind tunnels [8, 9] and numerical investigations performed with Large Eddy Simulations (LES) [7, 10, 11, 12] confirm the potential of the helix to increase the collective power output of two aligned turbines by up to 12.4 %, depending on pitch amplitude, excitation frequency and inflow conditions. Interestingly, in all the available literature, rotating the helix in a counter-clockwise direction (CCW) is more effective than rotating it in a clockwise direction (CW).

Several studies explored the underlying aerodynamic mechanisms to explain the enhanced wake recovery with the helix approach. First effects of the helix on features in the wake were observed in wind tunnel experiments regarding variations of the tip vortices' size, strength, and position [8, 9]. Using LES, Korb et al. [12] were the first to relate the power gains at downstream turbines to a lateral displacement of the wake caused by a deformation of the wake cross-section into a kidney shape. That kidney shape was later explained by two counter-rotating vorticity lobes established in the far wake by Coquelet et al. [11]. Gutknecht et al. [13] further investigated the vortex structures in the helix wake and observed the formation of a coherent helical vortex at the radial position of the wake boundary rotating in opposite direction for CW and CCW helix. In conjunction with the hub vortex, that helical vortex forms a system of co-rotating vortices in the CCW helix and counter-rotating vortices in the CW helix. These vortex systems eventually convert into the same counter-rotating vortex system in the far wake as observed by Coquelet et al. [11]. Relating the coherent vortices to the transport of mean kinetic energy into the wake, Gutknecht et al. [13] identified them as the governing driver for enhanced wake recovery and the difference between CW and CCW helix.

While the previously mentioned studies focused on the impact of the coherent vortex structures on the wake, this research adds to the field by (1) isolating the influence of the helix force perturbation on an axisymmetric porous disc wake, (2) identifying a co-rotating vortex system in the far wake and (3) conceptually comparing it to the vortex structures observed in the helix wake of a wind turbine to analyze effects related to blade phenomena, such as tip vortices, hub vortex, and swirl.

The isolated effect of the helix perturbation is obtained from Particle Image Velocimetry (PIV) measurements of porous disc (PD) wakes in a wind tunnel. These approximate the wake of a wind turbine in the far wake [14] without featuring blade-related phenomena in the near wake. Their cost-efficiency and low model complexity further establish PDs as the most suitable approach for isolating the effects of helix perturbation among available numerical and experimental wind turbine models. We use a simplified helix PD model developed by de Vos et al. [15], that mimics the force perturbation induced by the helix on the flow with a non-uniform porosity distribution over its surface. The dynamic nature of the helix is introduced by rotating it around its center with an electric motor. These results are compared to Large Eddy Simulations (LES) of a bladed turbine in laminar inflow.

The remainder of this paper first explains the helix porous disc model and its integration into the wind tunnel test setup in Section 2, followed by the analysis of the PD wakes and their comparison to the turbine wakes in Section 3 and closes stating the conclusions in Section 4.

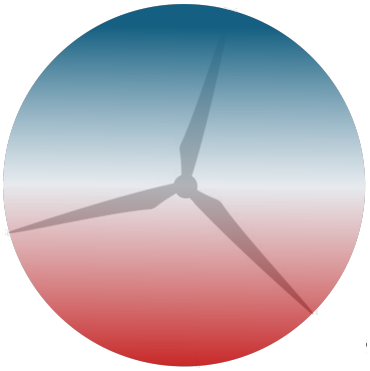

(a) Schematic of the thrust perturbation $\widetilde{F}_{T,Helix}(r,\phi,t)$ induced by the helix

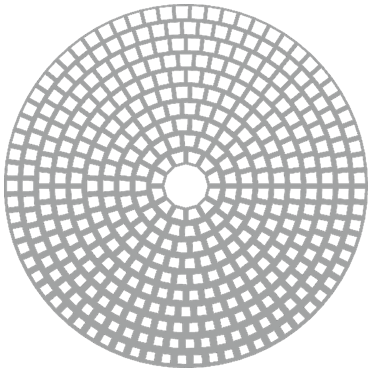

(b) Schematic of the helix porous disc model with non-uniform porosity distribution

(c) Helix porous disc model for wind tunnel testing

Figure 1: The concept of the helix porous disc model: Panel (a) schematically visualizes the areas of increased thrust over the rotorplane in red and of decreased thrust in blue at one time instance. That thrust distribution is mapped into the porous disc shown in panel (b). The reduced thrust regions correspond to regions of larger openings, and vice versa for the decreased thrust regions. In panel (c) the porous disc is mounted to a motor on a tower to obtain the turbine model used in the PIV experiments.

2 Methodology

This section starts by describing the concept of helix active wake control and how it is transferred into a simplified porous disc model. It proceeds with a description of the experimental wind tunnel setup and closes by outlining the LES setup for a bladed turbine.

2.1 Helix Active Wake Control

In the case of a conventionally greedy controlled wind turbine exposed to idealized uniform, laminar flow, the thrust force $F_{T,BL}(r)$ that the turbine exerts on the flow is symmetrically distributed over the rotor plane. It varies in radial direction r due to the non-uniform distribution of blade forces along the span but stays constant in the azimuthal direction ψ and over time t, creating an axisymmetric wake around the rotor center. Helix active wake control superimposes a dynamic, non-uniformly distributed force perturbation $\widetilde{F}_{T,Helix}(\psi,t)$ on the baseline thrust such that the actual thrust, the turbine exerts on the flow may be obtained as

$$F_T = F_{T,BL}(r) + \widetilde{F}_{T,Helix}(\psi,t). \tag{1}$$

$\widetilde{F}_{T,Helix}(\psi,t)$ is shaped such that the thrust on one side of the rotor is higher than on the other side, as schematically presented in Fig. 1a. Additionally, this perturbation rotates around the wake center either in the CW or CCW direction. As the flow propagates downstream, the wake deforms into the name-giving helical shape. Its rotational frequency expressed by the dimensionles Strouhal number $St = (f_e\, D)/U_\infty$, f_e being the excitation frequency and U_∞ the free wind speed, was found to govern the wake recovery enhancements.

This force perturbation is created by periodically pitching the blades with a phase offset, leveraging Individual Pitch Control (IPC). Accordingly, the blades decrease their pitch angle, which relates to an increase of the exerted force on the flow as they pass through the region of increased thrust and vice versa when they pass through the regions of decreased thrust. From a control perspective, that scheme is implemented by sinusoidally varying the fixed-frame tilt and yaw angles with a phase offset of $\pm 90°$, depending on CW or CCW rotation of the perturbation. These signals are then mapped into blade pitch signals $\beta_i(t)$ for each blade using a Multiblade Coordinate Transform (MBC), as described in detail by Frederik et al. [7].

2.2 Helix Porous Disc Model

De Vos et al. [15] derived a simplified helix model for wind tunnel testing by transferring the perturbed helix thrust force field into a porous disc with uneven porosity distribution. As presented in Fig. 1b, the regions of increased thrust force translate to regions of lower porosity (smaller holes) and the regions of

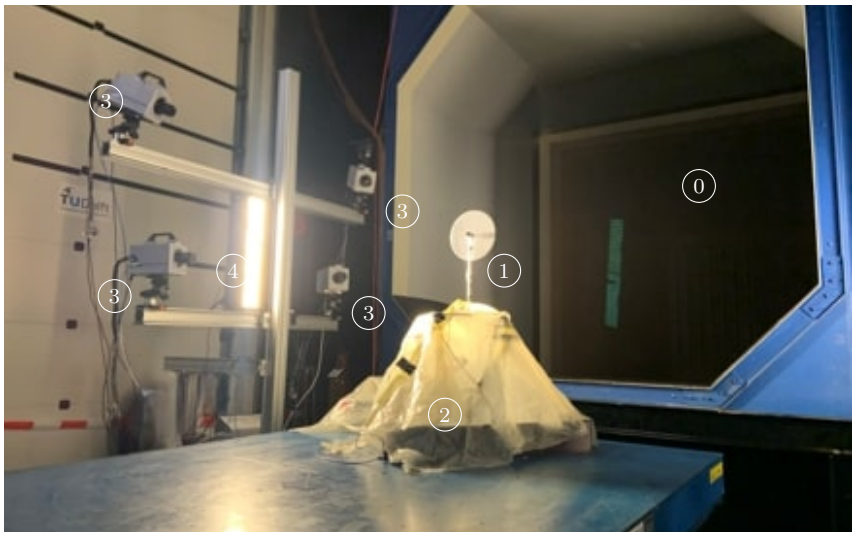

Figure 2: The experimental setup in the OJF with (0) beeing the outlet of the OJF, (1) the porous disc turbine model, (2) the hexapod, (3) the high speed cameras, (4) the LED Flashlights.

reduced thrust to regions of decreased porosity (larger holes). The dynamic excitation is then introduced by spinning the disc in CW or CCW direction using an electric motor. This approximates the nonuniform, unsteady deceleration the flow experiences as it passes through a bladed turbine applying helix active wake control. A detailed description of the design process of the helix porous disc is given in de Vos et al. [15]. Using smoke visualization techniques, they showed that the wake of their porous disc model deflects into a helical shape similar to the wake of a real turbine. Furthermore, the helix porous disc's wake recovers faster than a baseline disc's wake with uniform porosity distribution and the same total thrust. Similar to a bladed turbine, in the case of the porous discs, the Strouhal number governs the effectiveness of the helix. Thus, the helix porous disc model seems to trigger the same effect as the helix on a bladed turbine without adding the additional complexity of tip vortices, hub vortex, or unsteady blade effects. Therefore, it appears suitable for isolating the effect of the unsteady, non-uniform thrust distribution on a symmetric wake in this study.
In our experiments, we use a 3D-printed version of the helix porous disc with a diameter of $D_{PD} = 25$ cm. As rendered in Fig. 1c, the porous disc is mounted to a *Faulhabler AM2224R3* stepper motor that spins the disc with a rotational speed of $f_e = 3$ Hz. This corresponds to the optimal excitation Strouhal number identified by de Vos et al. [15] using a similar helix PD model of $St = 0.2$ in a free wind speed of $u_1 = 3.66$ ms^{-1}. The motor is covered with a 3D-printed housing to protect it from humidity that may settle on the motor due to the soap bubbles used as tracer particles. The motor is mounted to a 42 cm high aluminum tower.

2.3 Particle Image Velocimetry

The PIV experiments are performed in the closed-loop Open Jet Facility (OJF) at the Aerospace Engineering faculty of TU Delft. An electric fan with a power of 500 kW compresses the flow through an open jet with an octagonal outlet cross-section of 2.85 m × 2.85 m into the test section. Thereby, the flow experiences a contraction by a ratio of 3 : 1, which enables maximum wind speeds of 34 ms^{-1} at relatively low turbulence intensities TI. Lignarolo et al.[16] characterized the flow at $u_1 = 6$ ms^{-1} with $TI = 0.5$ % 1 m downstream the outlet and $TI = 2$ % at 6 m. This is consistent with van der Hoek et al. [9], who observed a turbulence intensity that slightly exceeds $TI = 2$ % at 2.5 m with $u_1 = 5$ ms^{-1}. The experiments in this work are performed with an inflow wind speed of $u_\infty = 3.66$ ms^{-1}, which is in the area of the previously mentioned flow characterizations and therefore allows to assume comparable TI levels in the range of ≈ 2 %.
Figure 2 shows the experimental setup used for the tomographic PIV in the OJF. The porous disc turbine model is placed on a hexapod (protected with a yellow plastic tarp) that only positions the porous disc closer to the center of the wind tunnel outlet. We use Helium Filled Soap Bubbles (HFSB) to visualize the flow, which, according to Scarano et al. [17] are suitable flow tracers for quantitative velocimetry in

Table 1: Overview of the cases measured with PIV

Case	Porous disc	St [ ]	rot. speed [Hz]	helix cycles
Baseline	uniform porosity	-	0	-
Helix CW	nonuniform porosity	0.2	3	30
Helix CCW	nonuniform porosity	0.2	3	30

wind tunnel experiments. The HFSB are introduced by a seeding rack placed upstream of the outlet jet of the OJF (not visible in Fig. 2) covering a crossflow area of 0.6 m $\times$ 0.9 m. The HFSBs are illuminated by two *LaVision LED Flashlights* to enable four *Photron FASTCAM SA 1.1* high-speed cameras to image the flow with a frame rate of 500 s^{-1} and a 1024×1024 pixels resolution. The cameras and flashlights are synchronized with a *LaVision PTU-X timing device*. Calibrating the PIV setup with a calibration plate followed by a volume self-calibration results in a geometrical mapping of the camera positions relative to the measurement domain. This allows the reconstruction of the particle positions with an error below 0.1 pixels. This setup can capture a volume of 1.6 $\times$ 2.8 $\times$ 2.8 D^3. To measure the entire wake region of interest in 0.5 D$< x <$ 4.5 D we subdivide it into three subdomains that partially overlap in x direction. For this purpose, the cameras and LED flashlights are mounted on a movable platform such that the entire setup can be moved in x direction with low effort. The investigated cases and their characteristics are summarized in Table 1.
The processing of the measured data is similar to van der Hoek et al. [9] and involves the following steps. First, the raw data is processed with the *LaVisions DaVis 10* software and then high-pass filtered to remove the background illumination. Then, the traces of the Lagrangian particle are reconstructed with the Shake-The-Box algorithm [18] and mapped onto a Cartesian grid with a cell size of 10 mm, by spatially averaging with a Gaussian weighting function. Since the seeding of the HFSBs is not entirely uniform in time and space, also the particle coverage of the measured domain varies. That may result in lower data accuracy at arbitrary time instances in partial regions of the wake. Due to the periodicity of the helix wake and the uniform inflow conditions, the severeness of the non-uniform particle coverage can be reduced by phase-averaging over 30 helix cycles at 72 phase instances.

2.4 Large Eddy Simulations

The symmetric PD wake represents a substantial simplification of the effect of the helix perturbation $\widetilde{F}_{T,Helix}(\psi, t)$ on a wake. Now, we go one level of complexity higher by comparing the effect of $\widetilde{F}_{T,Helix}(\psi, t)$ on the symmetric PD wake obtained from PIV to its effect on an asymmetric wind turbine wake featuring tip-vortices, hub vortex, and swirl. Therefore, we use the Large Eddy Simulations (LES) generated by Gutknecht et al. [13] with the LES wind turbine toolbox AMR-Wind [19] of an NREL 5 MW reference turbine [20] with a diameter of $D_{Turbine} = 126$ m. The turbine applies CW and CCW helix in uniform, laminar flow with a free wind speed of $u_\infty = 9$ ms^{-1}. The tilt-free turbine is centered in a crossflow direction in the domain and does not model tower, nacelle, and ground. Thus, the flowfields represent the effect of CW and CCW helix active wake control on the asymmetric turbine wake, isolated from the effects of turbulence, shear, or fluid-body interactions at solid turbine components. The turbine blades are modeled using the Actuator Line Method (ALM), and the domain is discretized with 80 cells per diameter in each spatial dimension. A detailed description of the LES Setup may be found in Gutknecht et al. [13].

3 Results

This section first presents the results of the PIV measurements of the PD wakes in terms of a mean flow analysis and an investigation of the phase-averaged features in the wake. It closes by comparing the coherent structures in the PD wakes to those in a turbine wake.

3.1 Mean Flow Analysis

We start by examining the effect of the helix perturbation on the wake recovery by analyzing the mean flow $\bar{u}_x$. For this purpose, we compute the effective wind speed $\mathcal{U}_{x,eff}$ a fully waked turbine would experience at various positions in the wake. This is obtained by averaging the mean wind speed $\bar{u}_x$ over the surface area shadowed by the rotor $\mathcal{S}_{rotor}$ as

$$\mathcal{U}_{x,eff} = \frac{1}{S_{rotor}} \iint_{S_{rotor}} \frac{\bar{u}_x}{\bar{u}_\infty} dS_{rotor}, \tag{2}$$

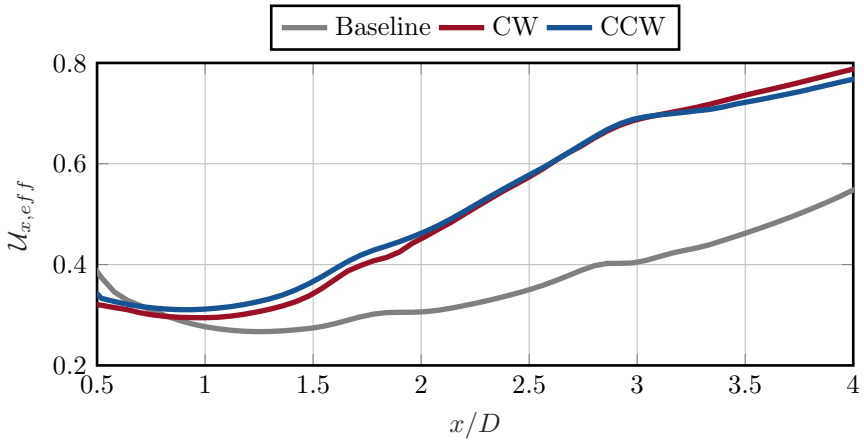

Figure 3: Effective wind speed a fully waked turbine would experience obtained by averaging over a circular surface of diameter D centered around the hub.

where $\bar{u}_x$ is obtained by averaging over 30 helix cycles and normalized with the free wind speed u_∞. Figure 3 compares the so-obtained $\mathcal{U}_x$ between the investigated cases. The helix and baseline PDs are designed to exert the same total thrust force F_T on the flow to make the recovery of the wakes comparable. Figure 3 reflects this, demonstrating equivalent effective velocities of $\mathcal{U}_{x,eff} \approx 0.3$ in the near wake region at $0.5 \leq x/D \leq 1$ across all investigated cases. Further downstream, the initially equal velocity deficit recovers faster for the helix cases than for the baseline, as indicated by a consistently higher effective wind speed throughout the entire investigated domain. Helix active wake control enhances the wake recovery within the same order of magnitude as observed on a bladed turbine [8, 9, 11, 13]. However, the trends observed at the PD differ from those on a bladed turbine in one decisive point. On a bladed turbine, the CCW helix consistently outperforms the CW helix throughout all the aforementioned studies. This discrepancy between CW and CCW helix is absent in the PD wakes as shown in Figure 3.
This observation points towards a causal distinction for different helix characteristics. First, the absence of the difference between CW and CCW helix was to be expected, since Gutknecht et al. [13] pinpoint the opposite alignment of the CW and CCW helix actuation with the always CCW-oriented wake swirl as the leading cause for their different performances. The wake swirl results from a deflection of the flow at the blades in the azimuthal direction against the sense of rotation of the rotor. The PDs do not model the blades; hence, their wakes do not inherit a swirling motion. Consequently, CW and CCW helix impose symmetric perturbations on the wake which apparently have similar effects on the mean flow. Thus, the equal effects of CW and CCW helix on the PD wakes confirm that the experimental setup is bias-free. Nevertheless, the major part of the wake recovery enhancement is still captured by the PD model. This indicates that the enhancement primarily arises from aerodynamic mechanisms triggered by the dynamic force perturbation that is equally present in the PD model as well as on a bladed turbine. The following sections investigate these aerodynamic effects in closer detail.

3.2 Phase-averaged features in the wake

We analyze the effect of the helix force perturbation on the shape of the PD wakes. For this purpose, Figure 4 visualizes hub height slices (left panel) and crossflow slices at $x = 4$ D (right panel) of the streamwise velocity u_x and the streamwise vorticity ω_x at one phase instance, phase averaged over 30 helix periods. The gray arrows in the crossflow slices indicate the crossflow velocity components. Even though the baseline wake does not feature an inherent periodicity, it is averaged at the same phase instances as the helix wakes to facilitate the comparability of the flow fields. The baseline wake reveals the expected axisymmetry, which is centered around the rotor hub and recovers its velocity deficit with increasing downstream distance from the PD. Regardless of the rotational direction of the helix perturbation, the wakes behind both helix PD cases deviate significantly from the symmetric baseline wake. The impact of the non-uniform porosity distribution may already be recognized in the near wake region ($x < 1$D) in the hub-hight slices. Whereas the baseline wake exhibits a symmetric velocity deficit on the upper and lower side of the wake, the helix wakes display a more pronounced velocity deficit on one side of the wake. This confirms that the non-uniform porosity distribution on the helix PDs leads, as intended,

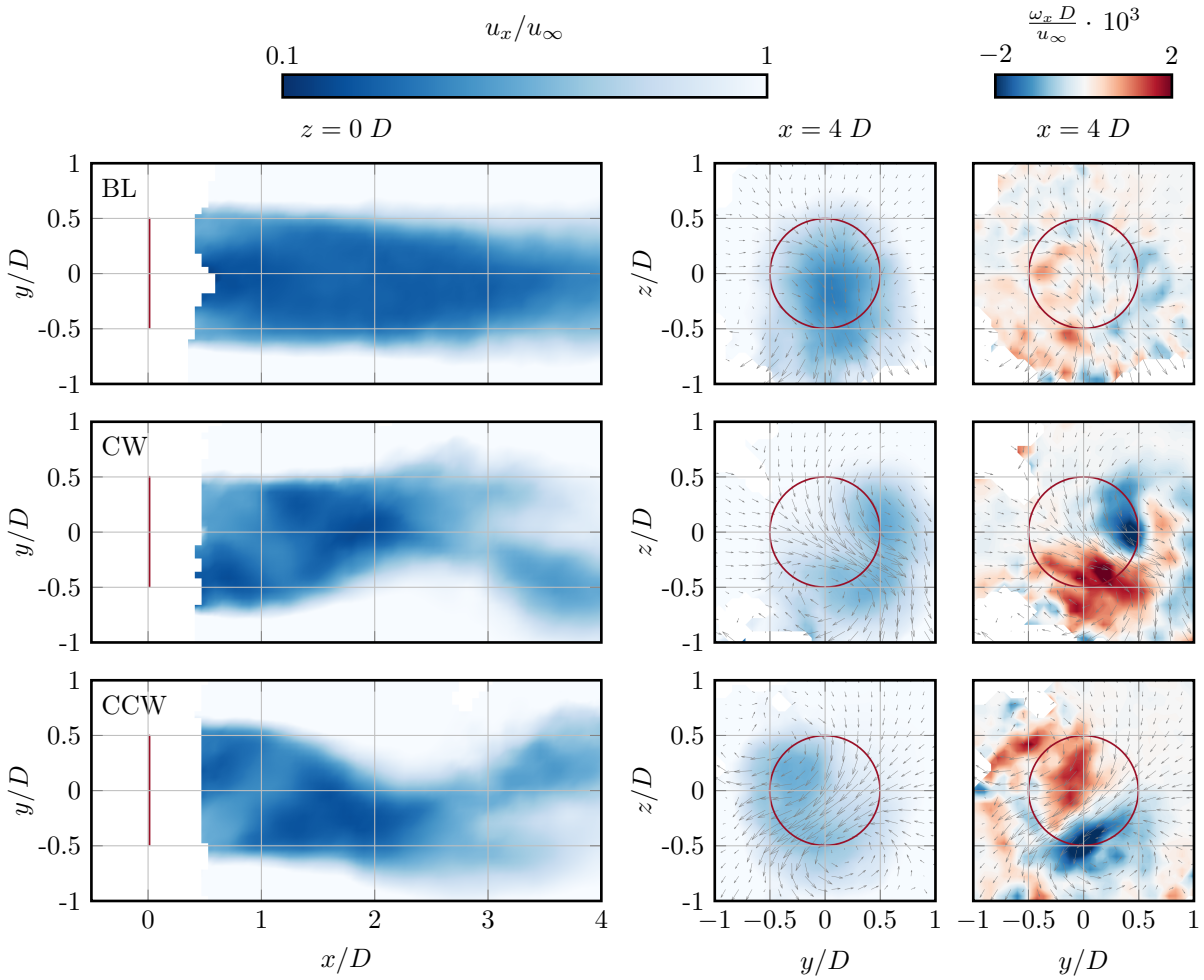

Figure 4: Flow fields at one phase instance at hub height in the left panel and at crossflow slices at $x = 4\ D$ in the right panel. The rotor area is indicated by the red line.

to an uneven flow deceleration over the rotor plane, similar as helix active wake control does at a real turbine. That near wake perturbation grows into a periodic deflection of the wake center up to 0.5D in the lateral direction as it propagates downstream. Thereby, the shape obtained from a CW and a CCW rotation of the helix PD appears symmetric.

The crossflow slices reveal that the lateral deflection comes with a deformation of the wake cross-section from a circular shape in the baseline case into a kidney shape in the helix cases. These kidney shapes are deflected in a crossflow direction and rotate around the wake center, generating the helical wake shape. The crossflow motions, indicated by the gray arrows, point to the cause of the kidney-shaped wake. The baseline wake features only small crossflow motions in the downward direction caused by an interaction of the flow with the support structure of the experimental setup. In contrast, the helix wakes inherit two vortex structures in the length scale of one rotor diameter located at opposite sides of the rotor surface. Their counter-rotating nature is further highlighted by the crossflow slices of streamwise vorticity ω_x in the right column of Figure 4, where two pronounced lobes of positive and negative vorticity indicate their position and rotational sense. Between each other, these vortices induce equally oriented crossflow motions that push the wake aside. The same mechanism, caused by a system of two, in that case static, counter-rotating vortices causes the lateral deflection of the wake at a yaw-misaligned turbine [14, 21, 22]. Similar kidney shapes caused by two counter-rotating vortex motions have been observed by Gutknecht et al. [13], Korb et al. [12] and Coquelet et al. [11] in the far wake of a conventional turbine applying the helix. This implies that the dominant driver for wake recovery enhancements achieved by the helix is due to a system

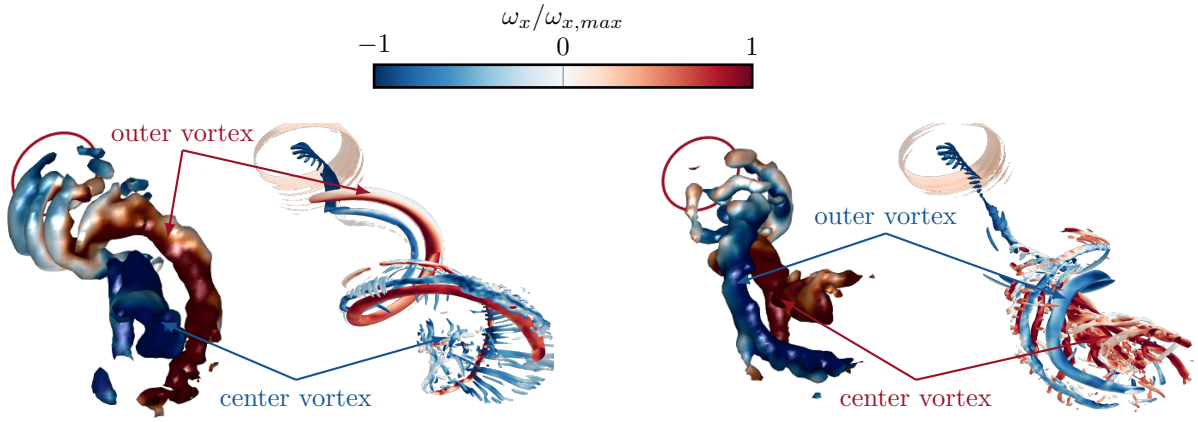

(a) PD, CW (b) Turbine LES, CW (c) PD, CCW (d) Turbine LES, CCW

Figure 5: Comparison of the vortex structures in the wake of the helix porous discs at one phase instance, obtained from PIV (a,c) and a bladed wind turbine applying helix active wake control (b,d) using isosurfaces of Q-Criterion. Case (a) and (b) apply the CW helix, and case (c) and (d) the CCW helix. The isosurfaces are colored by the streamwise vorticity ω_x to indicate the sense of rotation of the vortex. The turbine wakes were generated using LES by Gutknecht et al. [13].

of counter-rotating vortices that root in the dynamic force perturbation. Consequently, blade-related phenomena like tip vortices, hub vortex, or swirl are not required for their creation but might interact with them. The following section further investigates these interactions by comparing the structures in the PD wakes to the structures in a wind turbine wake.

3.3 Comparison of coherent structures to a bladed turbine

We proceed by analyzing the spatial structure of the counter-rotating vortices. Therefore, Figure 5 visualizes isosurfaces of the normalized Q-criterion, a common vortex identification method computed as

$$Q = \frac{U_\infty^2}{D^2}\frac{1}{2}(\Omega_{ij}\Omega_{ij} - S_{ij}S_{ij}) = -\frac{U_\infty^2}{D^2}\frac{1}{2}\frac{\partial u_i}{\partial u_j}\frac{\partial u_j}{\partial u_i} > 0, \tag{3}$$

where Ω_{ij} denotes the symmetric and S_{ij} the antisymmetric part of the velocity gradient tensor $\nabla\mathbf{u}$. Aside from the PD wakes obtained from the wind tunnel PIV experiments presented in panels (a) and (c), Figure 5 also visualize the helix wakes of a bladed turbine obtained from LES in panels (b) and (d). The turbine is centered in a crossflow direction in the domain, creating a point symmetric setup around the rotor center. This allows to increase the samples available for phase averaging by taking flowfields at distinct phase instances ϕ_i along a helix cycle and rotating them by $-\phi_i$ around the rotor center such that they correspond to the same phase instance. We consider four phase instances per helix period over ten periods, such that the phase averages shown in Figure 5 are obtained from 40 samples. This isolates the coherent structures related to the helix excitation frequency from structures related to different frequencies or random timescales.

The isosurfaces of the PDs correspond to $Q_{PD} = 2.14 \cdot 10^{-4}$, those of the LES of the turbine to $Q_{Turbine} = 2.04 \cdot 10^{-4}$. All the cases are spatially smoothed with a Gaussian filter. The isosurfaces are colored by the streamwise vorticity component normalized by its maximum value $\omega_x/\omega_{x,max}$ to indicate the sense of rotation of the vortex. A negative vorticity (blue) rotates in CCW direction (line of sight aligned with the direction of the free flow), and a positive vorticity (red) in CW direction. The obtained vortex structures allow for a conceptual comparison between PD wakes and turbine wakes, considering aspects like the overall structure and the rotational sense. However, the different origins of the data preclude a quantitative comparison.

The near wake, up to $x \approx 2\,D$ downstream of the helix PD (indicated by the red circle), is dominated by turbulent vortex structures shed from the edge of the PD. These shed vortices are particularly strong at the side of the increased induction zone. Further downstream, the shed vortices decay, and a vortex

system comprised of a helical outer vortex that spirals around an opposite rotating vortex located closer to the wake center establishes. That counter-rotating vortex system relates to the two counter-rotating vorticity lobes observed in Figure 4. The vortex system is symmetric for CW and CCW helix, i.e. that the outer and inner vortex flip their sense of rotation, as well as the handedness of the helical outer vortex when flipping the rotational direction of the helix force perturbation.
In both helix cases, the near wake of the turbines is dominated by the tip vortices, which are blurred into one vortex sheet due to the phase-averaging at the wake boundary and the CCW rotating hub vortex in the wake center. Further downstream, comparable coherent structures as in the PD wake arise. Clearly visible is the helical outer vortex that emerges at the wake boundary and spirals helically into the wake, following the rotation of the helix perturbation. The creation of the counter-oriented vorticity in the wake center is less clear as it comprises multiple smaller-scaled vortices rather than one coherent vortex. Even though the same features as in the PD wake may be observed, they lack the symmetry between CW and CCW helix. For instance, the outer vortex establishes further upstream in the CW wake than in the CCW wake, which indicates different growth rates until they reach the level identified by Q-Isosurfaces. In contrast, the wake center vortices appear more pronounced and further upstream in the CCW wake.
These observations suggest several insights into the aerodynamic mechanisms underlying the helix. First, they imply that the direct consequence of the helix force perturbation on a wake is the creation of two counter-rotating vortices, where one spirals helically around the other. In the case of a point-symmetric wake, like the PD wakes, these vortices react symmetrically to a change of the rotational direction of the force perturbation. Exposing an asymmetric wake, like a wind turbine wake, to the helix force perturbation creates the same overall vortex system, but manipulates its detailed characteristics. In the case of a wind turbine wake, the asymmetry created by the wake swirl first manipulates the growth rate of the outer vortex, notable by the changing locations at which the outer vortex can first be observed by means of Q-Isosurfaces. Furthermore, it affects the strength and shape of the vorticity created in the wake center. These asymmetric effects impact the wake recovery and consequently, the effectiveness of the helix for power optimization in windfarms as implied by the different effectiveness of CW and CCW helix in previous studies [7, 8, 9, 11].

4 Discussion and Conclusions

Previous studies have identified a system of coherent vortices to drive the accelerated recovery of a wind turbine wake exposed to helix active wake control. This work investigates the effect of the helix on a symmetric porous disc (PD) wake free from secondary effects present in a real turbine wake like tip vortices, hub vortex and swirl using Particle Image Velocimetry (PIV). The PD is modified to mimic the force perturbation of helix active wake control in a wind tunnel to investigate the aerodynamic mechanisms that accelerate the recovery of a wind turbine wake. The key takeaways of this study are that (1) the direct consequence of exposing a symmetric wake to the helix perturbation is the creation of two counter-rotating vortices composed of one vortex in the wake center and one helical vortex spiraling around it. That vortex system reacts symmetrically to changes in the rotational direction of the helix. (2) Asymmetries induced by tip vortices, hub vortex, and swirl break the symmetry between CW and CCW helix by unequally manipulating the growth rate and strength of the vortex structures.
Results show that the vortices created by CW and CCW helix equally enhance the mean velocity in the PD wakes. Both vortices induce equally oriented crossflow motions between each other that push the wake center aside, creating a kidney-shaped cross-section and entraining faster wind from the surrounding flow into the wake center.
Comparing these observations from the PD wakes to the helix wakes of a bladed turbine obtained from Large Eddy Simulations (LES) reveals that both inherit similar features in the far wake, like the helical outer vortex, vorticity created in the wake center, and a kidney-shaped cross-section. However, unlike the PDs, the turbine wakes react asymmetrically to CW and CCW actuation, causing the individual features to vary in specific characteristics, like their growth rate and intensity. These observations imply that the sole presence of the dynamic helix force perturbation suffices in accelerating a wake's recovery. Wake swirl, hub vortex, and tip vortices mutually interact with these mechanisms and thereby cause the difference between CW and CCW helix at a wind turbine. However, they do not participate in the primary triggering mechanism that facilitates the accelerated wake recovery.
It may be noted that this work is limited to a conceptual comparison between PD wakes and turbine wakes due to the fundamentally different data origins. Future work may focus on comparing both in similar simulation environments, preferably LES as it gives more freedom to customize the flow conditions and actuation settings as wind tunnel testing. This would allow for a more qualitative comparison of vortex strength, growth rate, and wake recovery to provide further insights into the interaction mechanisms of the helix perturbation with the secondary wake features. However, this requires an Actuator Disc Model

featuring the helix perturbation in an LES code. Following up on that, also the impact of turbulence, veer, and shear as present in a realistic atmospheric boundary layer could be examined.

Acknowledgments
This work is part of Hollandse Kust Noord wind farm innovation program where CrossWind C.V., Shell, Eneco, Grow and Siemens Gamesa are teaming up. Funding for the PhD's and PostDocs was provided by CrossWind C.V. and SiemensGamesa.

References

[1] Barthelmie R, Pryor S, Frandsen S, Hansen K S, Schepers J, Rados K, Schlez W, Neubert A, Jensen L and Neckelmann S 2010 *Journal of Atmospheric and Oceanic Technology*

[2] Doekemeijer B M, Kern S, Maturu S, Kanev S, Salbert B, Schreiber J, Campagnolo F, Bottasso C L, Schuler S, Wilts F, Neumann T, Potenza G, Calabretta F, Fioretti F and van Wingerden J W 2021 *Wind Energy Science* **6** 159–176

[3] Gebraad P M O, Teeuwisse F W, van Wingerden J W, Fleming P A, Ruben S D, Marden J R and Pao L Y 2016 *Wind Energy* **19** 95–114

[4] Bastankhah M and Porté-Agel F 2019 *Journal of Renewable and Sustainable Energy* **11** 023301 ISSN 1941-7012 URL `https://doi.org/10.1063/1.5077038`

[5] Fleming P, King J, Simley E, Roadman J, Scholbrock A, Murphy P, Lundquist J K, Moriarty P, Fleming K, van Dam J, Bay C, Mudafort R, Jager D, Skopek J, Scott M, Ryan B, Guernsey C and Brake D 2020 *Wind Energy Science* **5** 945–958

[6] Munters W and Meyers J 2018 *Wind Energy Science* **3** 409–425

[7] Frederik J A, Doekemeijer B M, Mulders S P and van Wingerden J W *Wind Energy* **23** 1739–1751

[8] Mühle F V, Heckmeier F M, Campagnolo F and Breitsamter C 2024 *Wind Energy Science* **9** 1251–1271

[9] van der Hoek D, den Abbeele B V, Simao Ferreira C and van Wingerden J W 2024 *Wind Energy* **27** 463–482

[10] Taschner E, van Vondelen A, Verzijlbergh R and van Wingerden J 2023 *Journal of Physics: Conference Series* **2505** 012006

[11] Coquelet M, Gutknecht J, Wingerden J V, Duponcheel M and Chatelain P 2024 *Journal of Physics: Conference Series* **2767** 092084 URL `https://dx.doi.org/10.1088/1742-6596/2767/9/092084`

[12] Korb H, Asmuth H and Ivanell S 2023 *Journal of Fluid Mechanics* **965** A2

[13] Gutknecht J, Taschner E, Coquelet M, Viré A and van Wingerden J W 2024 *Submitted to Physics of Fluids*

[14] Howland M F, Bossuyt J, Martínez-Tossas L A, Meyers J and Meneveau C 2016 *Journal of Renewable and Sustainable Energy* **8** 043301 ISSN 1941-7012 URL `https://doi.org/10.1063/1.4955091`

[15] De Vos B, Harder B M, Huisman T A, Gutknecht J and Van Wingerden J W 2024 *Journal of Physics: Conference Series* **2767** 092063 URL `https://dx.doi.org/10.1088/1742-6596/2767/9/092063`

[16] Lignarolo L, Ragni D, Krishnaswami C, Chen Q, Simão Ferreira C and van Bussel G 2014 *Renewable Energy* **70** 31–46 ISSN 0960-1481 special issue on aerodynamics of offshore wind energy systems and wakes

[17] Scarano F, Ghaemi S, Caridi G, Bosbach J, Dierksheide U and Sciacchitano A 2015 *Experiments in Fluids* **56** 42

[18] Schanz D, Gesemann S and Schröder A 2016 *Experiments in Fluids* **57**

[19] NREL 2024 Amr-wind `https://github.com/Exawind/amr-wind` accessed: 2024-07-23

[20] Jonkman J, Butterfield S, Musial W and Scott G URL `https://www.osti.gov/biblio/947422`

[21] Martínez-Tossas L A, Annoni J, Fleming P A and Churchfield M J 2019 *Wind Energy Science* **4** 127–138 URL `https://wes.copernicus.org/articles/4/127/2019/`

[22] Shapiro C R, Gayme D F and Meneveau C 2020 *Journal of Fluid Mechanics* **903** R2